

# Real-Space Phase-Field Simulation of Piezoresponse Force Microscopy Accounting for Stray Electric Fields

Lun Yang\* and Kaushik Dayal†

Civil and Environmental Engineering, Carnegie Mellon University

March 5, 2012

## Abstract

Piezoresponse Force Microscopy (PFM) is a powerful scanning-probe technique to characterize important aspects of microstructure in ferroelectrics. It has been widely applied to understand domain patterns, domain nucleation, and the structure of domain walls. In the article, we apply a real-space phase-field model to consistently simulate various PFM configurations. We model the PFM tip as a charged region that is external to the ferroelectric, and implement a boundary element method to efficiently and accurately account for the external stray fields that mediate the interactions between the tip and the ferroelectric. Our phase-field model and the solution method together are able to account for the electrical fields both within the specimen as well as those outside, and also consistently solve for the resulting electromechanical response with the same phase-field model. We apply this to various problems: first, the effect of crystal lattice orientation on the induced tip displacement and rotation; second, PFM scanning of a 90-degree domain wall that emerges at a free surface; third, the effect of closure domain microstructure on PFM response; fourth, the effect of surface modulations on PFM response; and fifth, the effect of surface charge compensation on PFM response.

**Keywords:** Piezoresponse Force Microscopy; Ferroelectrics; Phase-Field Modeling; Domain Walls; Boundary Element Method

## 1 Introduction

Ferroelectric materials are widely-used in sensors and actuators [1, 2], high-speed memory devices [3], microwave circuit elements [4, 5] and photonics [6, 7, 8] due to their attractive electromechanical and optical properties. Because these properties are strongly linked to microstructure and domain patterns, there has been much experimental effort to obtain an understanding of domain patterns at small scales. A leading experimental characterization tool that has been developed over the last decade is Piezoresponse Force Microscopy (PFM). The essential principle of Piezoresponse

---

\*luny@andrew.cmu.edu

†kaushik@cmu.edu

Force Microscopy is straightforward: an AC voltage applied through the tip of a conventional Scanning Probe Microscopy (SPM) excites the electromechanical (piezo) response of the ferroelectric, and the SPM then measures the superposition of local topography with the electromechanical distortion induced by the applied voltage. By keeping the frequencies of SPM scanning and the applied AC well-separated, the SPM measurement can be deconvolved to individually provide both topography as well as electromechanical distortion response. Thus, it is possible to obtain a spatial map of electromechanical response over the specimen surface, and from it an indication of domain patterns and other properties.

PFM has been successfully applied to a wide variety of settings and materials; important reviews of the development, implementation and challenge of PFM are [9, 10, 11]. A number of PFM modes have been developed: the vertical mode to measure the out-of-plane polarization based on induced displacements [12]; the lateral mode to measure the in-plane polarization based on induced angles [13]; and vector PFM that is a combination of both vertical and lateral PFM [14] to image the entire polarization vector at the surface. Based on these techniques, various measurements of domain patterns have been reported, e.g.  $180^\circ$  [15] and  $90^\circ$  [16, 17] domain patterns in ferroelectrics have been successfully observed. In addition, imaging of ferroelectric domains with high resolution was demonstrated when the PFM is used in an aqueous environment [18]. There have also been studies to image the detailed structure of both  $90^\circ$  and  $180^\circ$  domain walls [19, 20, 21].

Analytical models and numerical simulations have also been developed to provide guidance and support to PFM experiments. Simple analytical approaches are presented in [22, 23] to understand the intricate tip-surface contact. While these provides important insights, many approximations are necessary to enable a tractable analysis. For instance, the ferroelectric is dealt with as a homogeneous linear dielectric, and the bound charges and anisotropy that arise due to changes in the domain patterns induced by the tip are difficult to account for. In addition, the details of the domain pattern response to the applied field are unavailable. Numerical approaches based on phase-field modeling have also been used. Important contributions include [24] and [25]. In [24], they use phase-field modeling to simulate domain formation. However, they are forced to make significant approximations in their treatment of the electrical fields due to their inability to handle the external stray fields. Hence, the PFM tip is approximated roughly as flat electrodes directly on the specimen surface. In [25], they use semi-analytical approaches, and reach the important conclusion that the standard PFM approach to compute piezoelectric coefficients based on calibration against reference samples is questionable. While they are able to obtain important insights, the semi-analytical approach depends on additional approximations beyond the phase-field approach, and is also restricted in applicability.

The key difficulty in modeling PFM without any approximations beyond the phase-field model is the fact that the PFM tip with applied voltage is *outside* the specimen. Therefore, stray electric fields exist outside the ferroelectric specimen in vacuum. Hence, numerically, this requires the solution of the electrostatics equation on an infinite computational domain, simultaneously and consistently with the phase-field model that describes domain response to the applied field. We apply a boundary element method that enables efficient solution of the electrostatics equation by consistently transforming it to a finite domain [26, 27, 28] and couple this to the phase-field model. Hence, we are able to model a ferroelectric material in real-space with a complex mix of electrical and mechanical boundary conditions including those relevant to PFM [29].

We organize the article as follows. We present the phase-field model and numerical solution method

in Section 2. We apply this various questions of interest to PFM: first, the effect of crystal lattice orientation on the induced tip displacement and rotation, Section 3; second, PFM scanning of a 90-degree domain wall that emerges at a free surface, Section 4; third, the effect of closure domain microstructure on PFM response, Section 5; fourth, the effect of surface modulations on PFM response, Section 6; and fifth, the effect of surface charge compensation on PFM response, Section 7. Finally, we conclude and summarize the results in Section 8.

## 2 The Phase-Field Model and Numerical Solution Method

Following [30, 31, 32], the total potential energy  $E$  of a ferroelectric body  $\Omega$  (Fig.1) with elastic strain field  $\epsilon$  and the polarization field  $\mathbf{p}$  is written as:

$$E[\epsilon, \mathbf{p}] = \int_{\Omega} [U(\nabla \mathbf{p}) + W(\epsilon, \mathbf{p})] d\Omega + \frac{\epsilon_0}{2} \int_{\mathbb{R}^3} |\nabla \phi|^2 dV \quad (2.1)$$

Here,  $U$  penalizes gradients in  $\mathbf{p}$  and models the energy contributions from domain walls, and the stored (Devonshire) energy density  $W$  penalizes  $\mathbf{p}$  and  $\epsilon$  deviating from the spontaneous polarization and strain. The last term represents the electrostatic energy contained in the electric field  $\mathbf{E} = -\nabla \phi$ , where  $\phi$  is electric potential obtained from the electrostatic equation:

$$\nabla \cdot (\mathbf{p} - \epsilon_0 \nabla \phi) = 0 \quad \text{over } \mathbb{R}^3. \quad (2.2)$$

The first two terms in the energy (2.1) are local to the body being considered, while the electrostatic contribution is over all space.

The domain patterns in a ferroelectric can be described by fields  $\epsilon$  and  $\mathbf{p}$  that are local minimizers of  $E$ . Further, the response due to electric fields that are applied through the PFM tip is calculated by finding local minimizers of  $E$  with terms that account for external loads. This assumes that the frequency of the AC excitation is much lower than the timescales of electrostatics and elastodynamics respectively, i.e. the ferroelectric reaches mechanical and electrical equilibrium within a small fraction of an AC cycle. Such an assumption is standard in the field of PFM experiments and agrees with the estimated timescales for these phenomena.

We use tetragonal barium titanate in two-dimensions as our model material. Following [33, 34, 27, 35], we use for the energy:

$$\begin{aligned} U(\nabla \mathbf{p}) &= \frac{a_0}{2} (p_{1,1}^2 + p_{1,2}^2 + p_{2,1}^2 + p_{2,2}^2) \\ W(\epsilon, \mathbf{p}) &= \text{polynomial in } \mathbf{p} + \frac{1}{2} (\epsilon - \epsilon_T(\mathbf{p})) \cdot \mathbb{C} \cdot (\epsilon - \epsilon_T(\mathbf{p})) \end{aligned} \quad (2.3)$$

The details of the polynomial and other constants can be obtained from the references cited above.

These minimizers are numerically calculated by starting with assumed fields  $\epsilon, \mathbf{p}$  and evolving towards a minimum using a gradient descent. The gradient flow of  $E$  in the  $H_1$  norm is [36]:

$$\begin{aligned} \mu_1 \frac{dp_i}{dt} - \mu_2 \frac{d(p_{i,j})_{,j}}{dt} &= \left( \frac{\partial U}{\partial p_{i,j}} \right)_{,j} - \frac{\partial W}{\partial p_i} - \phi_{,i} \quad \text{over } \Omega \\ \left( \frac{\partial W}{\partial \epsilon_{ij}} \right)_{,j} &= 0 \quad \text{over } \Omega \\ p_{i,i} - \epsilon_0 \phi_{,ii} &= 0 \quad \text{over } \mathbb{R}^3 \end{aligned} \quad (2.4)$$

with  $\mu_1, \mu_2$  both non-negative.

Fig. 1 shows the mesh and the computational domain  $\Omega$ . The boundary conditions for the polarization evolution (2.4)<sub>1</sub> are  $\nabla \mathbf{p} \cdot \mathbf{n} = 0$  on all boundaries of the specimen, where  $\mathbf{n}$  is the outward normal to the boundary. The boundary conditions for mechanical equilibrium (2.4)<sub>2</sub> are traction-free on the top surface, and clamped on the other 3 faces. The clamping displacement is set to the value of the stress-free strain corresponding to a bulk crystal, to simulate the effect of the computational domain being embedded in a large bulk specimen on all sides except the top free surface. The boundary conditions for the electrostatics (2.4)<sub>3</sub> are grounded on the bottom and side faces, and voltage decays as the distance from the specimen tends to infinity. Similar boundary conditions have been used in our recent study of free-surface domain nucleation [29]. We start with an initial polarization field that we use to obtain the strain and electric potential from (2.4)<sub>2,3</sub>. We then update the polarization using (2.4)<sub>1</sub>. This process is repeated until convergence. The polarization update (2.4)<sub>1</sub> and mechanical equilibrium (2.4)<sub>2</sub> both use standard finite element methods (FEM) with triangle elements and linear shape functions, and polarization and displacement are the primary variables respectively.

The electrostatic equation (2.4)<sub>3</sub> needs attention as the electric fields are not confined to the ferroelectric but extend over all space. We model the tip as triangular with a uniform charge density  $\sigma$  above the specimen. Hence, it is important to account for the electric fields in vacuum and they cannot be neglected as they mediate the tip-ferroelectric interactions. We apply a Dirichlet-to-Neumann boundary element method to solve this infinite domain problem efficiently and accurately, as described in [26, 28]; in particular, [28] describes an iterative formulation that is particularly suited for nonlinear coupled problems such as arise here. While the details of the method are discussed in these references, the essential aspect of the method is that it consistently transforms the Neumann-type boundary conditions from the charge on the tip and the bound charge in the ferroelectric to the Dirichlet-type boundary conditions of potential specified on the boundary of the ferroelectric  $\Omega$ , Fig. 1. This enables us to then solve (2.4)<sub>3</sub> using standard FEM.

The raw signal from a PFM experiment is simply the superposition of tip displacement due to specimen surface topography and tip displacement due to piezoresponse. These signals are however at very different frequencies, and can be deconvolved by a lock-in amplifier. Hence, the final output regarding piezoresponse consists of two specific pieces of information: (i) the amplitude of the sinusoidal tip displacement due to piezoresponse from applied sinusoidal AC signal (ii) and the phase difference between the sinusoidal tip displacement response and the sinusoidal applied AC signal. Because damping is typically assumed small, the phase difference is either 0 or  $\pi$  radians, depending on the sign of the piezoresponse, and is readily calculated. The main quantity of interest here is the amplitude of the tip displacement. Because only amplitude is measured and not the entire cycle, for our simulations it suffices to examine only the maximum voltage of the simulated AC cycle as this leads to the maximum response (unless large-scale switching occurs). Therefore, to calculate the amplitude of the PFM response signal, we simply apply the charge/voltage corresponding to the amplitude of the applied AC at the spatial position of the tip, and compute  $\epsilon$  and  $\mathbf{p}$  that are local minimizers of  $E$  with accounting of applied loads. The polarization  $\mathbf{p}$  provides the dielectric response, and the strain field  $\epsilon$  can be used to compute the displacement beneath the tip that is measured. In addition,  $\epsilon$  provides the slope at the surface, which is related to the twisting of the PFM tip that has been the focus of recent PFM studies. The slope provides a means to distinguish the in-plane direction of the spontaneous polarization.



Finally, we note that we only examine the positive maximum of the applied electric field amplitude. This is sufficient because the system is symmetric with respect to a change in sign of both the applied electric field and the polarization vector together.

### 3 Effect of Lattice Orientation on PFM Tip Induced Displacements and Angles

We first study PFM scanning the surface of a single domain ferroelectric specimen with the crystalline lattice at various angles to the free surface. There is a well-understood mapping that enables deduction of the both out-of-plane and in-plane polarization directions from the PFM induced/measured tip displacements and tilt for  $a$ - and  $c$ -axis domains, i.e. when the spontaneous polarization is aligned perfectly tangential and perfectly normal to the free surface respectively [10]. However, when the spontaneous polarization is between these extremes, it is not clear how to deduce these from PFM. Our simulation can provide some insight. In addition, the extreme cases of  $a$ - and  $c$ -axis provide validation for the method.

We denote the angle of the crystal lattice with the horizontal direction to be  $\theta$ . We start from an in-plane polarization direction ( $\theta = 0^\circ$ ), and increase  $\theta$  in steps of  $15^\circ$  until  $90^\circ$ . At each of these angles, we compute the induced displacement and angle (slope) directly beneath the tip, Fig. 2. When there exists an initial displacement/angle before application of the electric field from the tip, this is subtracted to find the induced displacement/angle.

We find in Fig. 2(a) that the PFM induced displacement increases linearly until  $\theta \simeq 60^\circ$ , followed by a gradual leveling-off beyond that. On the other hand, the PFM induced angle does not show much of a linear region at all, Fig. 2(b), but rather the slope of the curve continually increases in magnitude as it goes towards 0 at  $\theta = 90^\circ$ . From Fig. 2, we can conclude that it is difficult to distinguish between a  $c$  domain ( $\theta = 90^\circ$ ) and a domain with  $\theta = 75^\circ$  from the induced displacement alone; however, the difference in induced slope is significant and the tilt of the PFM tip can resolve these two cases. Similarly, it is hard to differentiate an  $a$  domain ( $\theta = 0^\circ$ ) from a domain with  $\theta = 15^\circ$  by the induced angles alone, but in conjunction with the induced displacement it is possible to tell these cases apart.

While in practice it is unlikely that our simulations will achieve quantitative accuracy, the trends are likely to be reliable. Hence, by calibrating against a reference sample with known crystal lattice orientation, the plots in Fig. 2 can potentially provide quantitative guides to deduce crystal lattice orientations from PFM measurements.

### 4 PFM Signature of a Single $90^\circ$ Domain Wall

The second example we study is to apply the PFM tip above a simple  $90^\circ$  domain of ferroelectrics. The initial domain pattern is shown in Fig. 3: a  $90^\circ$  domain wall that separates an  $a$ -domain from a  $c$ -domain. The domain wall is compatible both mechanically and electrostatically. As we move the PFM tip, the induced displacements and angles on the sample surface are measured at various locations, shown in Fig. 4. It is important to note that the plots in Fig. 4, and similar plots for

other domain patterns, are *not* the distortions of the free surface for a *fixed* tip position, but instead the distortion directly beneath the tip for various tip positions. Mathematically, if we write the tip position  $T$  as a function of time  $t$ , i.e.  $T(t)$ , and we write the displacement field  $\mathbf{u}(\mathbf{x}, t)$  as a function of position  $\mathbf{x}$  and time  $t$ , then we are *not* plotting  $u_2(x_2 = 0, x_1, t = t_0)$  vs.  $x_1$ ; rather we are plotting  $u_2(x_2 = 0, x_1 = T(t), t = t)$  vs.  $T(t)$  for various times  $t$ . The latter is precisely the output of a PFM scan. Here, subscripts refer to coordinate directions, 1 being horizontal and 2 being vertical. In addition, time  $t$  is simply a parameter since we do not consider truly dynamic processes. Also note the 2 tip positions on either side of the domain wall marked “1” and “2”.

Our calculations show some interesting features. First, the induced displacements for  $a$  polarization is much smaller than  $c$  polarization, while the induced angles are much larger for  $a$  polarization than the  $c$  polarization. This result matches well with experiment and is independent of the applied electrical amplitude  $\sigma$ . Here, we note that  $\sigma$  is non-dimensionalized such that dielectric breakdown is roughly  $O(10^4)$ . Second, we see an asymmetric signature of the  $90^\circ$  wall. This shows a complexity that is usually not considered when analyzing experimental measurements to obtain domain wall thickness, e.g. [19, 20]. In addition, we note that even over the  $a$  domain the induced displacement is significantly different from 0 due to interference from the  $c$  domain beneath it. Third, we note the snapshots of domain patterns in Fig. 5 for different tip strengths  $\sigma$  at locations 1 and 2. For  $\sigma = 0.4$ , the polarization at location 1 rotates upwards only slightly, Fig. 5(a); however, for  $\sigma = 1.2$ , Fig. 5(b), a new domain forms under the PFM tip, giving rise to a large induced displacement. At location 2, we see that the response is much simpler and the polarization primarily only changes in magnitude, Figs. 5(c) and 5(d). Therefore, not only is the domain wall signature more complex than the usual  $\tanh(\cdot)$  solution in the bulk, it is also sensitive to the magnitude of the applied voltage even in regimes that are nominally completely linear.

## 5 PFM Signature of Closure Domains

We next examine PFM scanning of the surface of a specimen with closure domains. Closure domains form at free surfaces if the bound surface charge is not compensated [26, 34]. The initial domain pattern and the direction of PFM tip motion is shown in Fig. 6. The domain pattern is a combination of both  $a$  and  $c$  domains that minimizes surface bound charge and is compatible in the interior.  $a$  domains form near the surface to minimize the electrostatic energy from the surface charge  $\mathbf{p} \cdot \mathbf{n}$ . Beneath this,  $c^+$  and  $c^-$  domains exist and are separated by  $180^\circ$  domain walls.

Fig. 7 compares the induced displacements for various  $\sigma$  as the PFM scans the specimen. Because the  $a$  domain dominates the surface, the displacements are small except for location 1. At location 1, the electric field from the tip causes an increase in size of the existing  $c^-$  domain, Figs. 8(a) and 8(b). Thus, the displacement is large at location 1 compared with the other locations, and increases with  $\sigma$ . Figs. 8(c), 8(e), 8(d) and 8(f) compare the domain patterns at locations 2 and 3 for different  $\sigma$ . When  $\sigma = 0.4$ , the polarization rotates a little without any new domains nucleating. When  $\sigma = 1.2$  however, new  $c^-$  domains nucleate. However, since the tip is above a large  $a$  domain, the displacements are relatively small for both locations 2 and 3.

## 6 PFM Signature of Closure Domains with Surface Modulation

We next examine PFM scanning above the surface of closure domains with surface modulation. Closure domain patterns with surface modulation have been modeled by phase-field simulation without any surface charge compensation [34]. The domain patterns and the direction of tip motion is shown in Fig. 9.

Fig. 10 compares the displacements for various  $\sigma$  as the PFM scans the specimen. Similar to Section 5, the displacement is small except for locations 1 and 5. For the same reason that the tip field promotes the enlargement of the  $c^-$  domain, the PFM induced displacement is large in location 1 and 5. Further, as in the flat surface case, the displacement increases with  $\sigma$  at location 1. However, location 3 shows a  $c^-$  domain nucleated due to the tip above the original  $c^+$  domain inside the specimen, resulting in a relatively larger response compared to the flat surface case, Fig. 10. The domain patterns at locations 1, 3, and 5 are shown in Fig. 11. The asymmetry due to the surface modulation provides different closure domain patterns at different locations, such as at the peak and the valley [34]. This is reflected in the asymmetry of Fig. 10 around location 3. We also see that the displacement is positive for  $\sigma = 0.4$  but becomes negative for  $\sigma = 0.8$  and  $\sigma = 1.2$  at location 3.

## 7 Effect of Surface Charge Compensation

We now examine the effect of surface charge compensation on PFM scanning signatures above closure domains. There are different proposed mechanisms for charge screening, e.g. [37, 38], but it is not completely clear whether screening is intrinsic or extrinsic. However, different charge compensation mechanisms can cause completely different domain patterns at the free surface. Therefore, we use three distinct compensation models and examine the PFM signature of each of these.

The three surface compensation models are: (i) complete compensation from a layer of charges inside the specimen; (ii) complete charge compensation from a layer of charges outside the specimen; and (iii) partial charge compensation from outside the specimen. In case (i), the compensation is to model the semiconductor nature of ferroelectrics [38] and the free charges inside the material are likely to move to the surface under the electric field generated from ferroelectric closure domain patterns. Cases (ii) and (iii) correspond to compensation by charged species from the ambient surroundings [37].

In (i), we set the total compensating charge to be equal to the bound surface charge  $\mathbf{p} \cdot \mathbf{n}$ , and the charges are uniformly distributed over a layer extending from the surface to 50nm below the surface. This results in the polarization near the surface reducing in magnitude and forming a depletion-like layer near the surface, shown in Fig. 12(a). In (ii), we set the total compensating charge to be equal to the bound surface charge  $\mathbf{p} \cdot \mathbf{n}$ , but the charges are uniformly distributed over a layer extending from the surface to 5nm above the surface. This results in distinct  $c^+$  and  $c^-$  domains, shown in Fig. 12(b). In (iii), we set the total compensating charge to be equal to  $0.4\mathbf{p} \cdot \mathbf{n}$ , distributed as in (ii). Fig. 12(c) shows a domain pattern between complete closure and case (ii). In each case, as the tip field is applied, the compensating charge is held fixed at the original values even as the polarization at the free surface evolves in response to the applied field. This is reasonable because space charge transport is typically much slower than the PFM cycling frequency.

The tip displacement and tilt are shown in Fig. 13 for the 3 cases. The displacement curves almost coincide in cases (i) and (iii), though the domain patterns at the surface are completely different in these cases. However, model (ii) has much larger induced displacements at all points except when the tip is directly above the  $180^\circ$  domain wall. When the tip is directly above the domain wall, all models show almost no piezoresponse. This can be expected because the displacements result primarily from the normal component of polarization at the surface due to the  $d_{33}$  effect. The domain patterns for each model are shown in Figs. 14, 15 and 16 for various tip locations. At location 1, the domain patterns in Fig. 15(a) for model (ii) indicate a larger displacement compared to Figs. 14(a) and 16(a) for models (i) and (iii) respectively. On the other hand, at location 4, the induced  $c^-$  domain on top of the original  $c^+$  domain in Figs. 14(c) and 16(c) results in a smaller induced negative displacement than Fig.15(c) for similar reasons to those described in Section. 5.

Physically, the reasons for the difference can be summarized thus: in model (i) with compensation in the interior, the response is small because the compensation at the surface reduces the magnitude of the polarization; in model (iii) with partial compensation in the exterior, the response is small because  $a$  domains dominate; and in model (ii) with complete compensation in the exterior, the response is large. Hence, though the physical mechanisms behind models (i) and (ii), and the resulting closure domain patterns, are very different, they show similar PFM signatures though for different reasons.

Fig. 13 also shows the tip tilt as a function of position. As expected there is not much tilting directly above the  $c^\pm$  domains, but we can see a clear signature of the domain wall. There is extremely good qualitative agreement with corresponding experiments in [13], where they present PFM tilt measurements of  $180^\circ$  walls in lithium niobate. Given that we are modeling barium titanate, quantitative agreement is not expected. A particular feature that stands out is that in the partially compensated case, model (iii), the  $a$ -domains play a significant role between locations 3 and 4, and cause the tilt angle to change sign from that expected in models (i) and (ii) with no  $a$ -domains. Our calculations of tip displacement profile near the domain wall also match very well with these experiments. In addition, the profiles also match well with simpler analytical approaches [23], however, an important advantage is that we can directly examine the domain pattern as it is influenced by the applied field, Figs. 14, 15 and 16.

## 8 Conclusion

We have presented a phase-field method to simulate the PFM signatures of various complex domain patterns. The method relies on a consistent use of a phase-field model as the only physical input, combined with a real-space numerical technique based on boundary elements to account accurately and efficiently for the external stray fields. This enables us to consider the complex geometry corresponding to an electric field applied through a PFM tip located outside the ferroelectric specimen. Our method accounts for the tip-specimen interactions through the stray fields, while simultaneously and consistently finding the induced domain patterns.

We apply the method to a number of situations of current interest to the use of PFM: (1) the effect of crystal lattice orientation on the induced tip displacement and rotation; (2) PFM scanning of a  $90^\circ$ -degree domain wall that emerges at a free surface; (3) the effect of closure domain microstructure on PFM response; (4) the effect of surface modulations on PFM response; and (5) the effect of

surface charge compensation on PFM response.

In (1), we calculate the induced tip displacement and rotation for various angles of crystal lattice orientation, potentially providing a quantitative tool for deducing polarizations other than the extreme  $a$  and  $c$  domains. In (2), we find that the signature of a  $90^\circ$  domain wall is both asymmetric as well as sensitive to applied field strength. In (3), we examine the spatial characteristics of the signature of a complex closure domain pattern. In (4), we calculate the differences from (3) if the free surface is not flat but instead spatially modulated. Finally, in (5), we examine the effect of 3 different models of charge compensation on the PFM signature of a closure domain. One model corresponding to intrinsic compensation, and the other two corresponding to partial and complete extrinsic compensation respectively. We find that though the physical mechanisms and the domain patterns of intrinsic compensation and partial extrinsic compensation are very different, the resulting PFM signatures are similar.

## Acknowledgment

This research was supported in part by the National Science Foundation through TeraGrid resources provided by the Pittsburgh Supercomputing Center. The real-space phase-field program that we have developed to obtain the results described in this paper is available at [www.matforge.org](http://www.matforge.org).

## References

- [1] Xu, Y. (1991) *Ferroelectric materials and their applications*, North-Holland, .
- [2] Uchino, K. (1996) *Piezoelectric Actuators and Ultrasonic Motors*, Kluwer, .
- [3] Scott, J. (2000) *Ferroelectric memories*, Springer Verlag, .
- [4] Tagantsev, A. K., Sherman, V. O., Astafiev, K. F., Venkatesh, J., and Setter, N. (2003) *J. Electroceram.* **11**, 5–66.
- [5] El-Naggar, M. Y., Dayal, K., Goodwin, D. G., and Bhattacharya, K. (2006) *J. Appl. Phys.* **100**, 114115.
- [6] Ferraro, P., Grilli, S., and De Natale, P. (2008) *Ferroelectric crystals for photonic applications: including nanoscale fabrication and characterization techniques*, Springer Verlag, .
- [7] Wessels, B. (2007) *Annu. Rev. Mater. Res.* **37**, 659–679.
- [8] Dayal, K. and Bhattacharya, K. (2007) *J. Appl. Phys.* **102**, 064102.
- [9] Gruverman, A. and Kalinin, S. (2006) *Journal of Materials Science* **41(1)**, 107–116.
- [10] Kalinin, S., Rodriguez, B., Jesse, S., Karapetian, E., Mirman, B., Eliseev, E., and Morozovska, A. (2007) *Annu. Rev. Mater. Res.* **37**, 189–238.

- [11] Kalinin, S., Rar, A., and Jesse, S. (2006) *Ultrasonics, Ferroelectrics and Frequency Control, IEEE Transactions on* **53(12)**, 2226–2252.
- [12] Kalinin, S. and Bonnell, D. (2002) *Physical Review B* **65(12)**, 125408.
- [13] Johann, F., Jungk, T., Lilienblum, M., Hoffmann, Á., and Soergel, E. (2010) *Applied Physics Letters* **97**, 102902.
- [14] Kalinin, S., Rodriguez, B., Jesse, S., Shin, J., Baddorf, A., Gupta, P., Jain, H., Williams, D., and Gruverman, A. (2006) *Microscopy and Microanalysis* **12(3)**, 206–220.
- [15] Streiffer, S., Eastman, J., Fong, D., Thompson, C., Munkholm, A., Ramana Murthy, M., Auciello, O., Bai, G., and Stephenson, G. (2002) *Physical review letters* **89(6)**, 67601.
- [16] Ganpule, C., Nagarajan, V., Li, H., Ogale, A., Steinhauer, D., Aggarwal, S., Williams, E., Ramesh, R., and De Wolf, P. (2000) *Applied Physics Letters* **77**, 292.
- [17] Abplanalp, M., Eng, L., and Gunter, P. (1998) *Applied Physics A: Materials Science & Processing* **66**, 231–234.
- [18] Rodriguez, B., Jesse, S., Baddorf, A., and Kalinin, S. (2006) *Physical review letters* **96(23)**, 237602.
- [19] Shilo, D., Ravichandran, G., and Bhattacharya, K. (2004) *Nature Materials* **3(7)**, 453–457.
- [20] Franck, C., Ravichandran, G., and Bhattacharya, K. (2006) *Applied physics letters* **88(10)**, 102907–102907.
- [21] Tian, L., Vasudevarao, A., Morozovska, A., Eliseev, E., Kalinin, S., and Gopalan, V. (2008) *Journal of Applied Physics* **104(7)**, 074110–074110.
- [22] Felten, F., Schneider, G., Saldana, J., and Kalinin, S. (2004) *Journal of applied physics* **96**, 563.
- [23] Morozovska, A., Eliseev, E., Bravina, S., and Kalinin, S. (2007) *Physical Review B* **75(17)**, 174109.
- [24] Ng, N., Ahluwalia, R., Su, H., and Boey, F. (2009) *Acta Materialia* **57(7)**, 2047–2054.
- [25] Pan, K., Liu, Y. Y., and Li, J. Y. (2011) *submitted*.
- [26] Dayal, K. and Bhattacharya, K. (2007) *Acta Materialia* **55(6)**, 1907–1917.
- [27] Yang, L. and Dayal, K. (2010) *Applied Physics Letters* **96**, 081916.
- [28] Yang, L. and Dayal, K. (2011) *Journal of Computational Physics* **230(21)**, 7821 – 7829.
- [29] Yang, L. and Dayal, K. (2012) *Journal of Applied Physics, in press*.
- [30] Shu, Y. and Bhattacharya, K. (2001) *Philosophical Magazine Part B* **81(12)**, 2021–2054.

- [31] Li, L., Lei, C., Shu, Y., and Li, J. (2011) *Acta Materialia*.
- [32] Li, L., Yang, Y., Shu, Y., and Li, J. (2010) *Journal of the Mechanics and Physics of Solids* **58(10)**, 1613–1627.
- [33] Zhang, W. and Bhattacharya, K. (2005) *Acta materialia* **53(1)**, 185–198.
- [34] Yang, L. and Dayal, K. (2011) *Acta Materialia* **59(17)**, 6594 – 6603.
- [35] Xiao, Y., Shenoy, V., and Bhattacharya, K. (2005) *Physical review letters* **95(24)**, 247603.
- [36] Yang, L. and Dayal, K. (2012) *International Journal of Fracture*, *in press*.
- [37] Kalinin, S. and Bonnell, D. (2001) *Physical Review B* **63(12)**, 125411.
- [38] Watanabe, Y., Okano, M., and Masuda, A. (2001) *Physical Review Letters* **86(2)**, 332–335.

## Figures

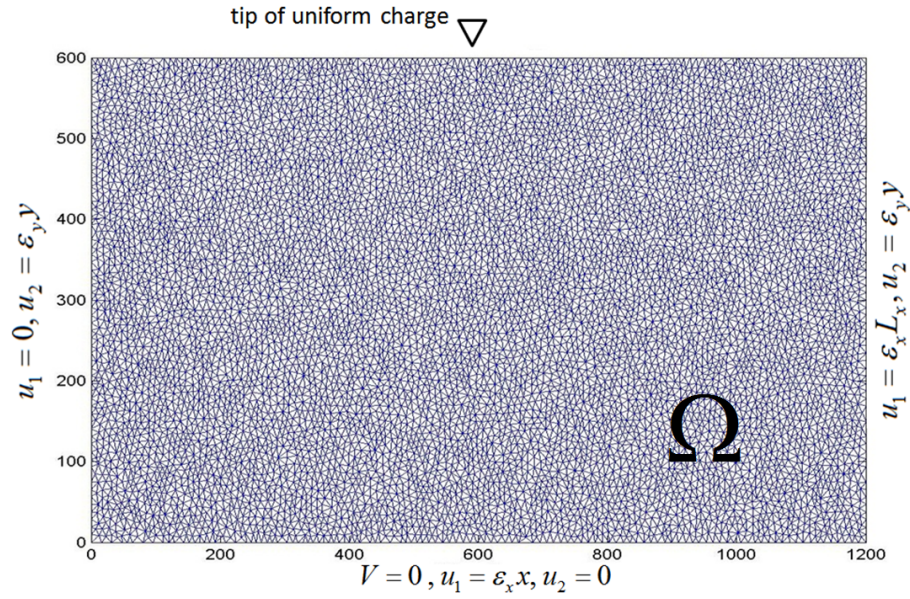


Figure 1: Domain discretization and boundary conditions.

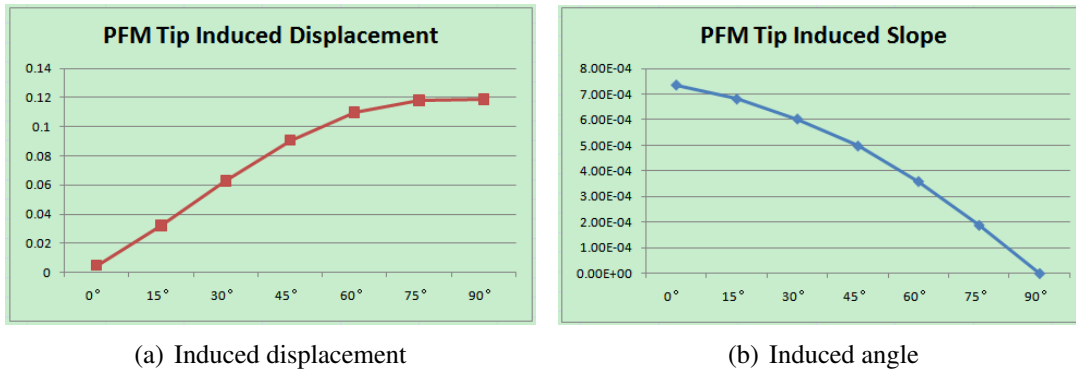


Figure 2: Induced displacement and angle for a single domain as a function of crystal lattice orientation  $\theta$ . The displacement and angle correspond to the distortion of the sample surface directly beneath the PFM tip.



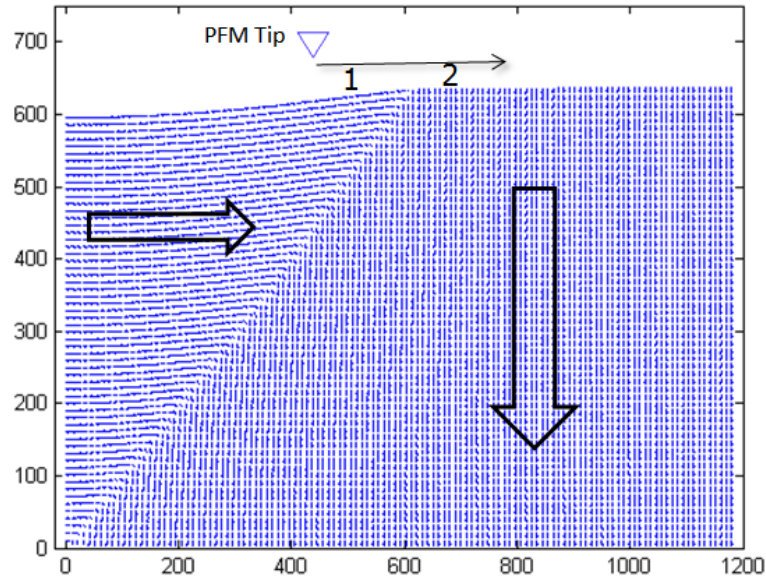


Figure 3: A  $90^\circ$  domain wall. The arrow shows the direction of PFM movement, and locations 1 and 2 are examined in detail.

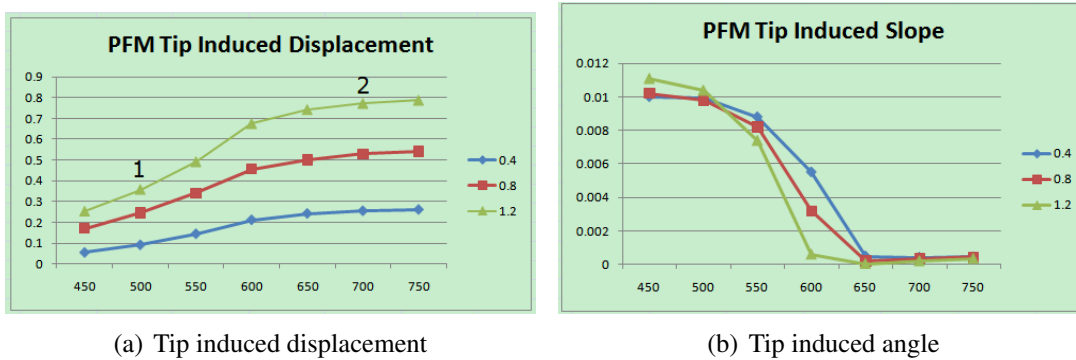


Figure 4: Induced displacement and angle for a single  $90^\circ$  domain wall for various applied field amplitude  $\sigma$ . It is important to note that these and following figures are *not* plots of the shape of the free surface, but plots of displacement directly beneath the tip for various tip positions.

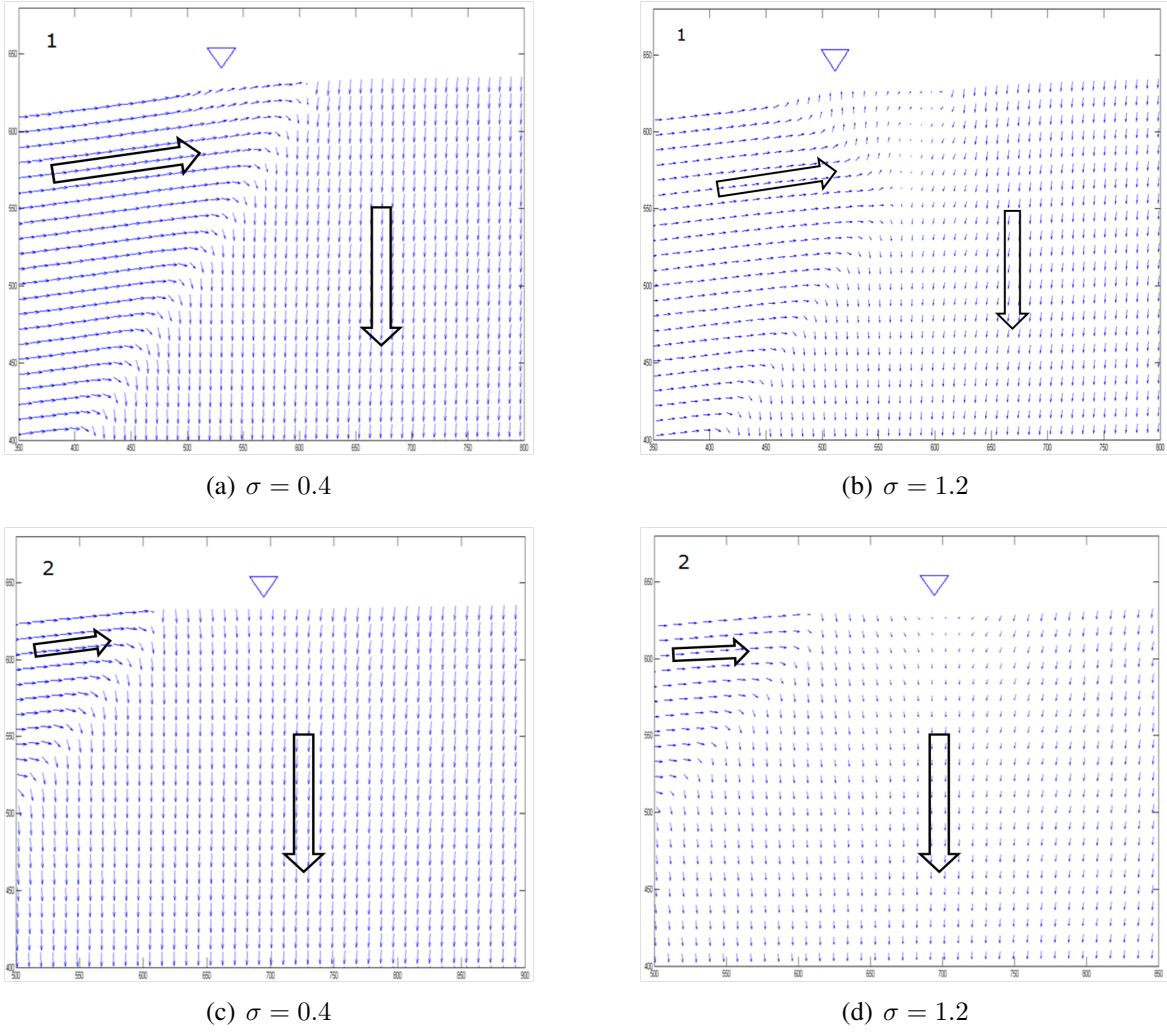


Figure 5: Domain patterns for different tip locations (shown by the triangle) and applied field amplitudes  $\sigma$ .

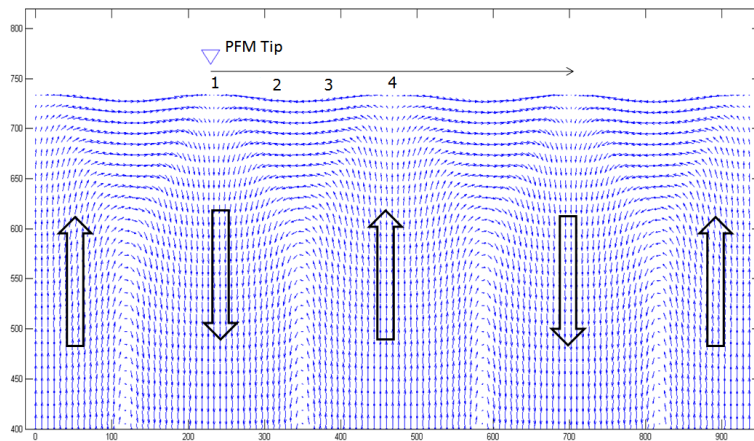


Figure 6: Closure domain patterns. Locations 1, 2, 3, 4 are examined in detail.

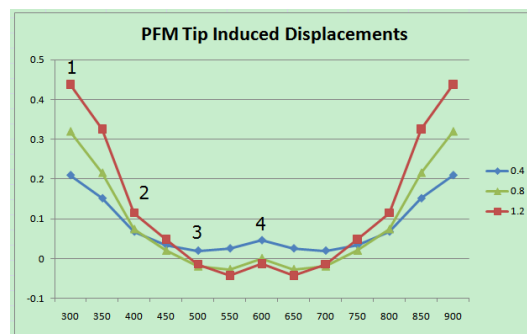


Figure 7: Induced displacement for closure domains under various applied field strengths  $\sigma$ .

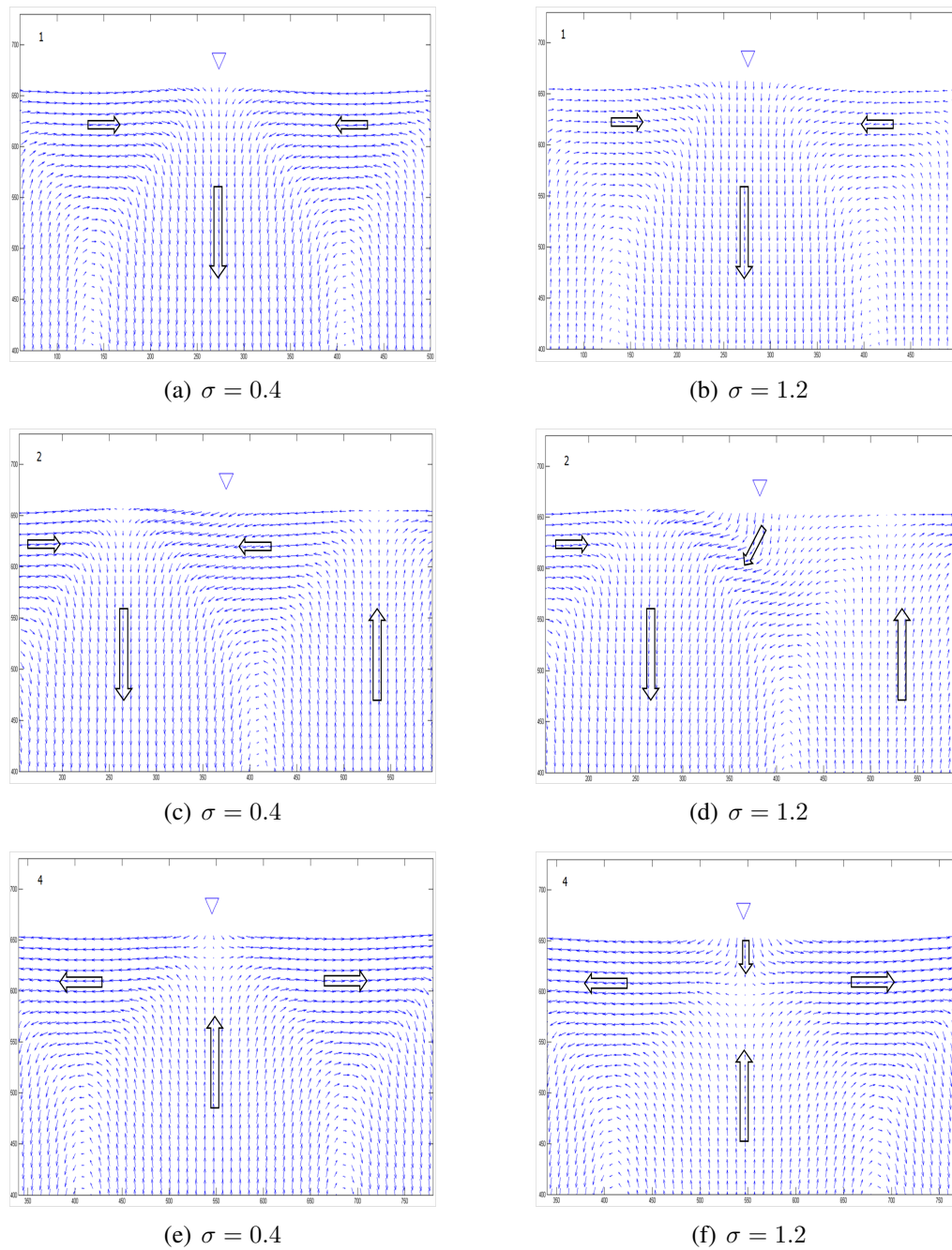


Figure 8: Domain patterns for closure domains under various applied field strengths  $\sigma$ .

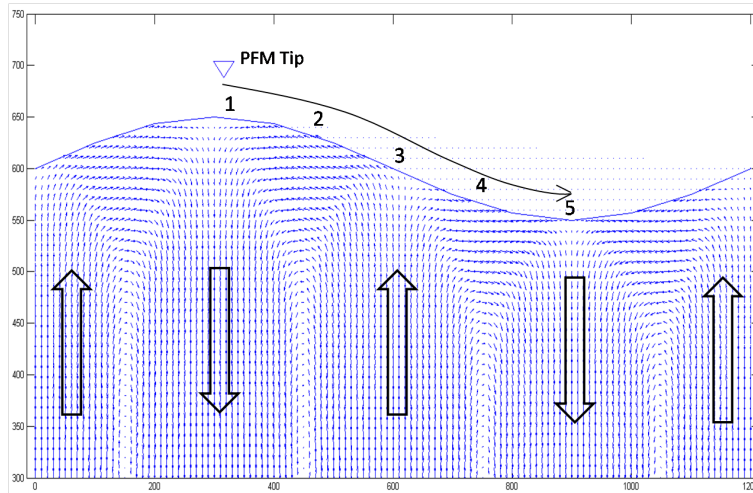


Figure 9: Closure domain patterns at a modulated free surface. Locations 1, 2, 3, 4, 5 will be examined in detail.

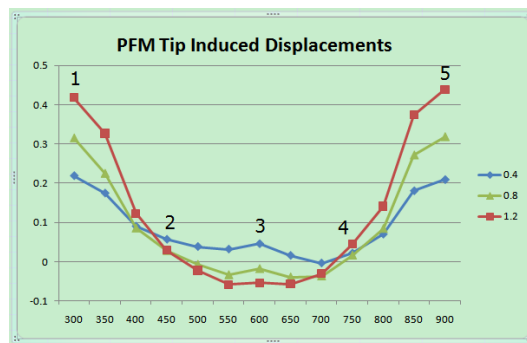


Figure 10: Induced displacement for closure domains with surface modulation with various applied field strengths  $\sigma$ .

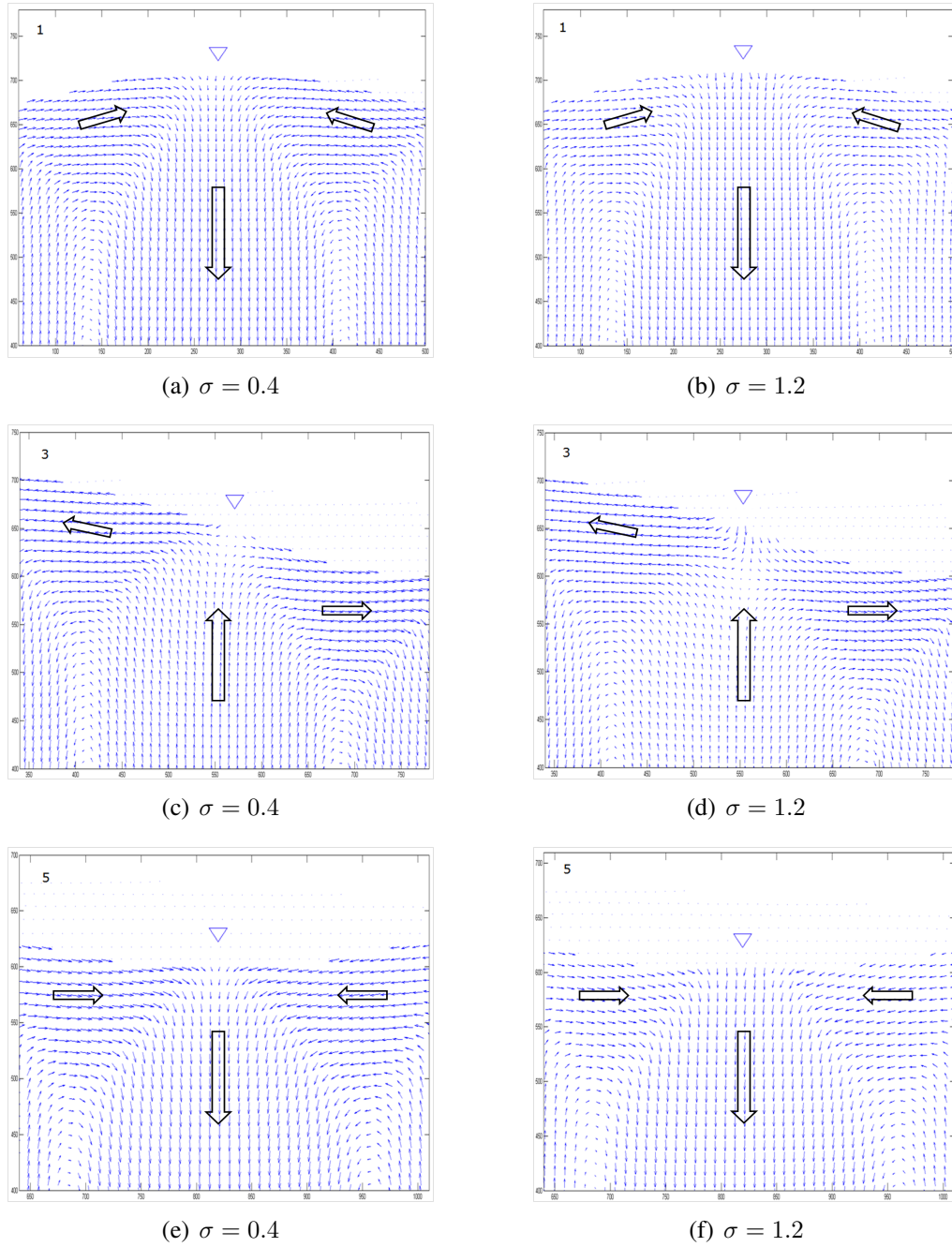
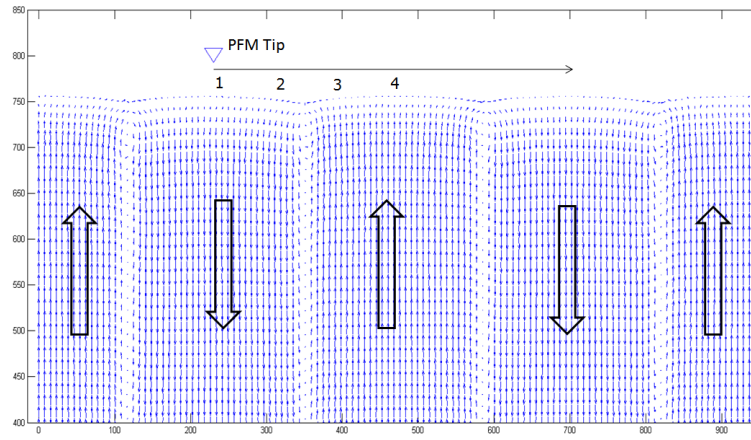
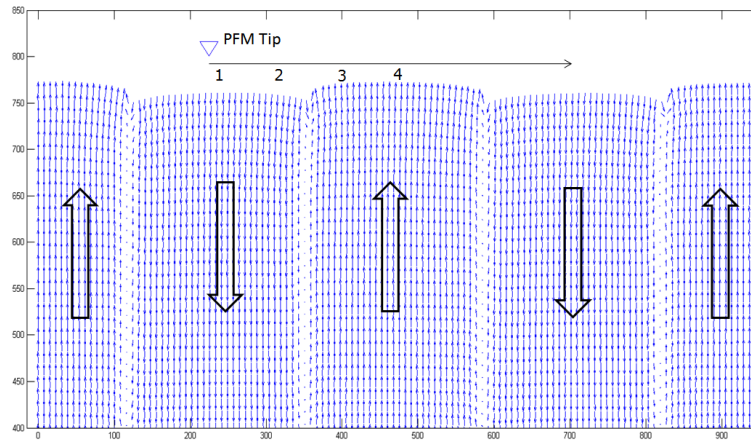


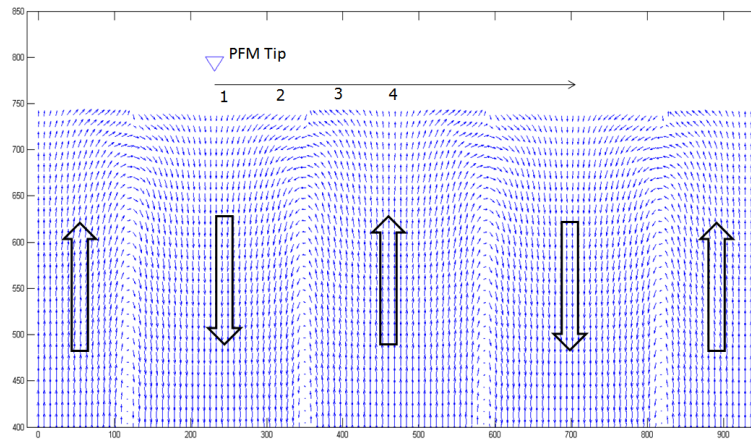
Figure 11: Domain patterns under the PFM tip for closure domains with surface modulation for different  $\sigma$ .



(a)



(b)



(c)

Figure 12: Closure domain patterns with different surface charge compensations. (a) Model (i): complete surface charge compensation in the interior of the specimen. (b) Model (ii): complete surface charge compensation in the exterior of the specimen (c) Model (iii): partial surface charge compensation in the exterior of the specimen.





Figure 13: Induced displacements and slopes for the different surface charge compensation models.

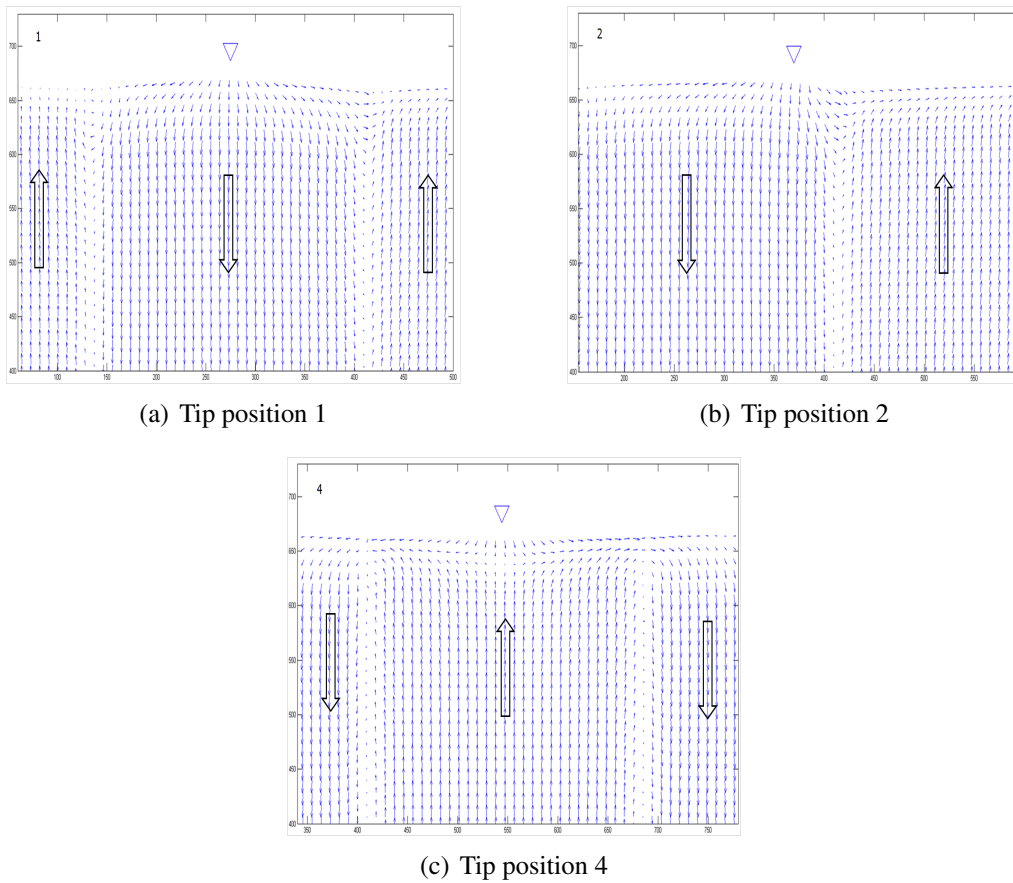


Figure 14: Domain patterns with surface charge compensation using model (i) for different PFM tip positions.



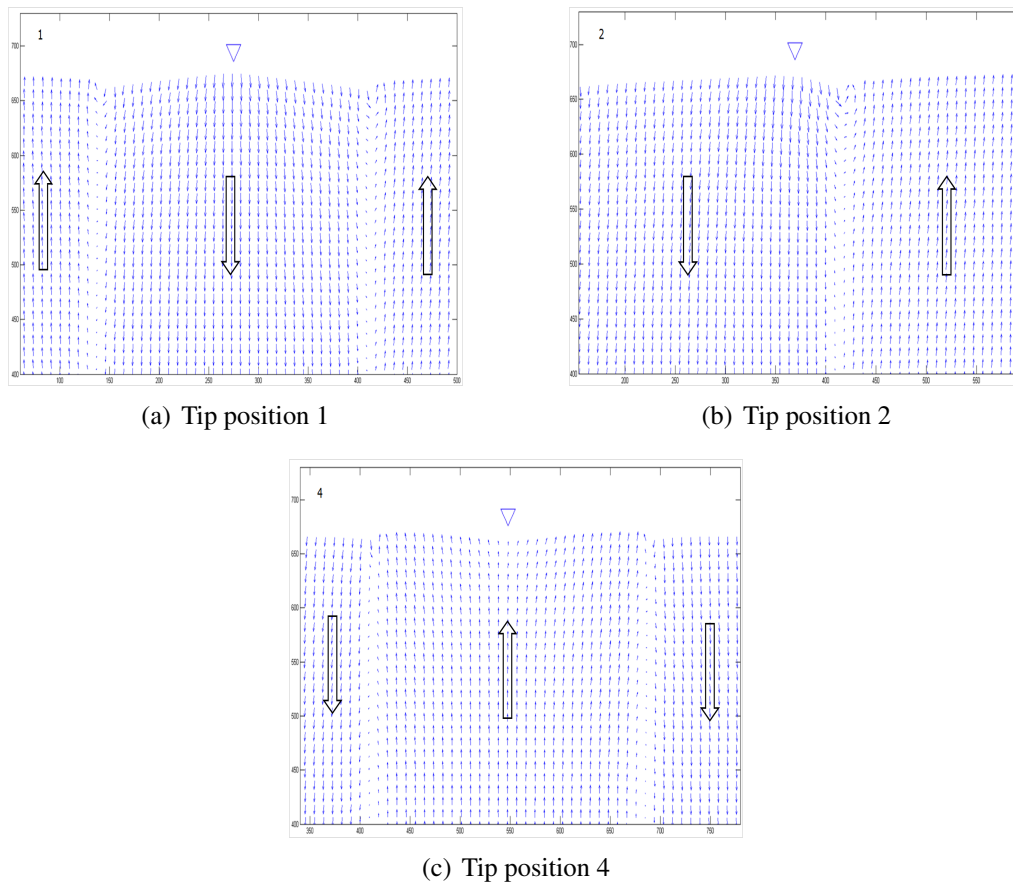


Figure 15: Domain patterns with surface charge compensation using model (ii) for different PFM tip positions.

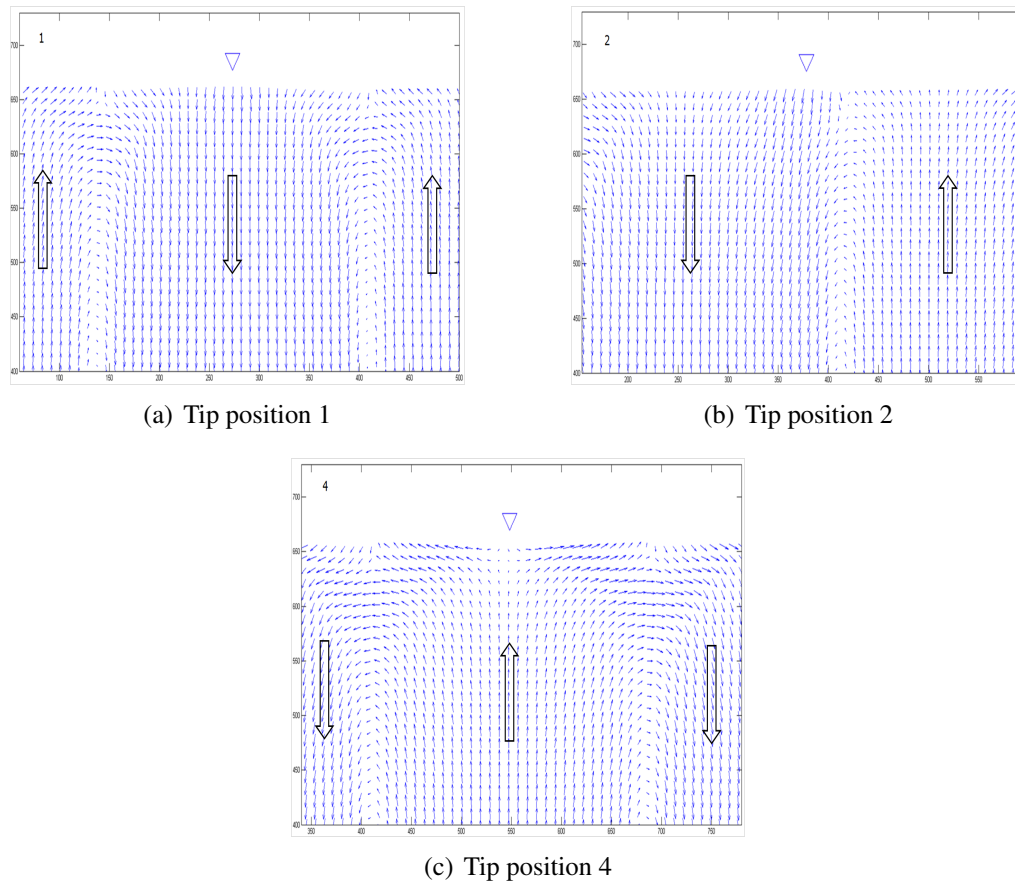


Figure 16: Domain patterns with surface charge compensation using model (iii) for different PFM tip positions.